Chapter 10
Diagnosing Intense and Ultra-intense Laser–Matter Interactions: Status and Future Requirements

Leonida A. Gizzi

Abstract In this chapter we describe experimental techniques for investigating laser–matter interactions that have been developed in recent years within the framework of international collaborations. We introduce phenomena observed in the wide range of interaction regimes and plasma conditions, including long-scale-length plasmas, laser–plasma coupling in inertial fusion studies, and electron acceleration driven by ultrashort pluses. We focus on laser–matter interactions, particularly laser–solid interactions and laser–gas jet interactions. We also discuss in details the temporal and spatial features of laser pulses amplified by the chirped pulse amplification (CPA) technique (Strickland and Mourou, Opt. Commun. 56:212, 1986) with special attention to the properties that play an important role in laser–solid interactions, including pulse duration, contrast, prepulses and focusing configurations.

We investigate plasma formation and plasma density evolution by optical interferometry techniques. We also discuss techniques for recovering information on plasma density evolution when optical interferometry with ultrashort pulses is adopted. Further, we introduce time-resolved X-ray spectroscopy of plasmas generated by ultrashort laser pulses, then we describe recent measurements of fast electron transport in solids conducted by using a novel monochromatic imaging technique. Finally, we briefly analyze some future instrumentation requirements for investigating laser–matter interaction when femtosecond laser pulses are adopted.

10.1 Introduction on Ultra-Intense Laser–Matter Interactions

When an intense, short laser pulse is focused on a solid target, several features of the pulse have to be considered because there are many mechanisms that can take place, and the dominating ones need to be identified. Among others, consideration needs

L.A. Gizzi
Intense Laser Irradiation Laboratory, Istituto Nazionale di Ottica, Consiglio Nazionale Delle Ricerche, Area della Ricerca CNR, Via G. Moruzzi, 1 – 56124 Pisa, Italy
and
INFN, Pisa, Italy

K. Yamanouchi (ed.), *Lectures on Ultrafast Intense Laser Science 1*, Springer Series in Chemical Physics 94, DOI 10.1007/978-3-540-95944-1_10,

to be given to the prepulse features, long pulse to short pulse contrast, prepulses, and so on. As discussed later in the chapter, one of the key applications of intense, short laser pulses is the *fast ignition* (FI) approach [1, 2] to *inertial confinement fusion* (ICF) where ultrahigh intensity interaction is used to generate energetic (MeV) electrons that propagate in the compressed core and initiate the nuclear fusion reactions. In these circumstances, there is a great interest in understanding how fast electrons are produced, how they propagate in the target substrate, how they transfer their energy to the compressed material, what is the production efficiency, and what fraction of their energy can be dumped in the target. All these features depend strongly on the conditions that the laser pulse finds on the target surface; and after generation of the electrons begins, their transport will be affected by several mechanisms, including the electron beam parameters and the resistivity of the material.

This leads us to take a close look at CPA lasers. In typical CPA systems based upon Ti:Sa, a nJ-level femtosecond, ultrashort laser pulse, generated by an oscillator, is stretched in a dispersive medium (e.g., optical fiber, gratings) to reach the sub-ns pulse duration. As shown in Fig. 10.1 for the case of the ILIL laser system at INO-CNR, in these systems a stretched seed pulse is preamplified by a high-gain preamplifier, typically a so-called *regenerative amplifier*. The mJ level pulse thus generated is further amplified in a multipass configuration and then optically compressed, typically using a grating compressor. A view of the multipass amplifier (right) and of the vacuum compressor of the femtosecond laser system at ILIL taken during test operations using a remotely controlled camera is shown in Fig. 10.2.

In general, such lasers are characterized by the so-called *pedestal*, due to *amplified spontaneous emission* (ASE), which is characterized by a nanosecond temporal duration. Then, there are some features of the pulse that arise from limitations in the optical compression of the stretched, amplified laser pulse due to grating imperfections. Finally there are low energy pre- and postpulses and, of course, the main pulse.

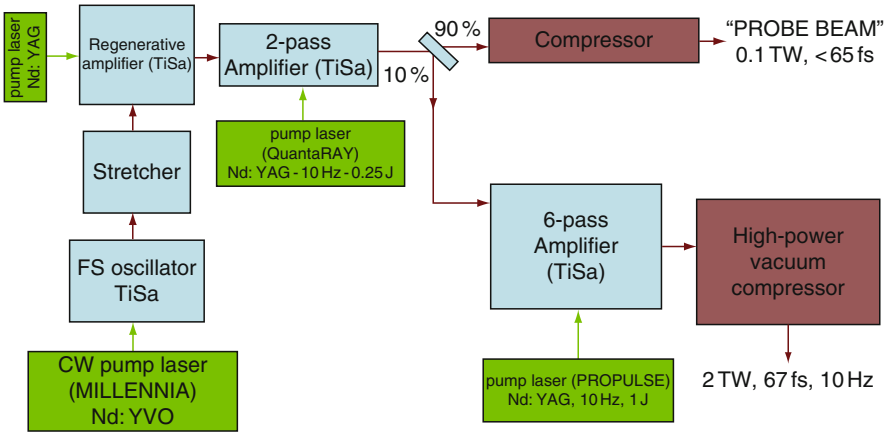

Fig. 10.1 Schematic layout of the FIXER femtosecond laser system at ILIL, showing the front-end and the power amplifier

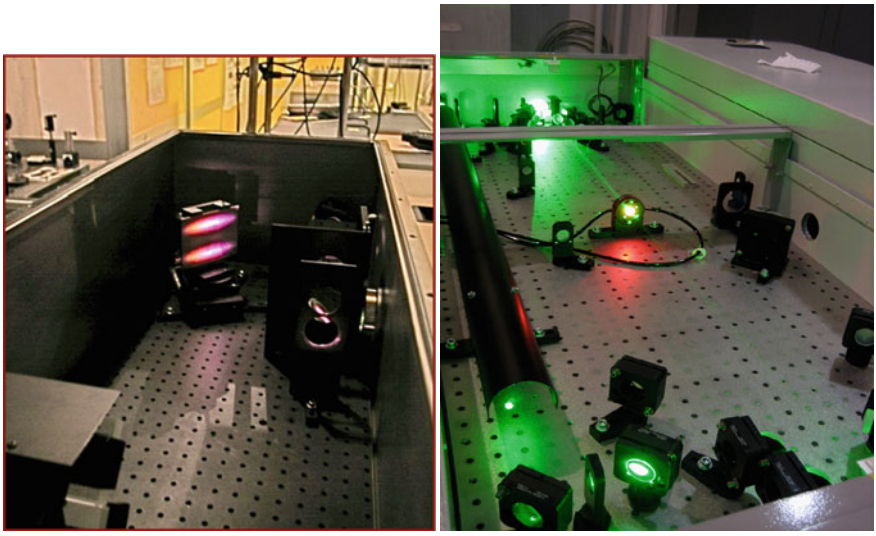

Fig. 10.2 Images of Ti:Sa femtosecond FIXER laser system at the ILIL lab at INO-CNR, Pisa. On the *right* is a view of the 6-pass amplifier showing the pumping beams (*green*) and the fluorescence of the Ti:Sa crystal (*red*). On the *left* is a view of the inside of the vacuum compressor showing one of the gratings with the patterns of the forward- and backward-propagating 800 nm beam

The most important feature to be considered in CPA laser–target interactions is indeed the ASE that can deliver a significant amount of energy on target before arrival of the main short pulse, at intensity that can lead to premature plasma formation [3]. The temporal profile of a typical CPA pulse appears as seen in Fig. 10.3 with the ASE contrast, i.e., the ratio of the peak intensity to the ASE intensity ranging from 10^5 to a best performance of 10^{10} in recent, contrast enhanced systems. For high focused intensities of up to $10^{20}\,\mathrm{W/cm^2}$, the ASE level will range approximately from a minimum of 10^{11} to a maximum of $10^{15}\,\mathrm{W/cm^2}$. In the case of interactions with solid targets, these intensities generate a precursor plasma on the target. If no measures are taken to prevent this, the CPA pulse will interact with the preformed plasma generated by the ASE rather than with the solid target surface.

Recently, effective techniques have been developed to suppress precursor radiation and prepulses to increase the contrast. With regard to ASE, one of these techniques is the plasma mirror, the effectiveness of which has been established by recent experiments with ultrathin foil targets [4]. Presently, the only drawback of this technique is the limited repetition rate because the surface on which the plasma mirror is generated has to be replaced at every shot.

Figure 10.4 shows an example of a more realistic temporal profile obtained from a third-order cross-correlation measurements of the front end (10 mJ) output of the FIXER (Femtosecond Interaction X-ray Emitter) laser system. In this case the pulse is compressed after a two-stage amplifier including the regenerative amplifier and

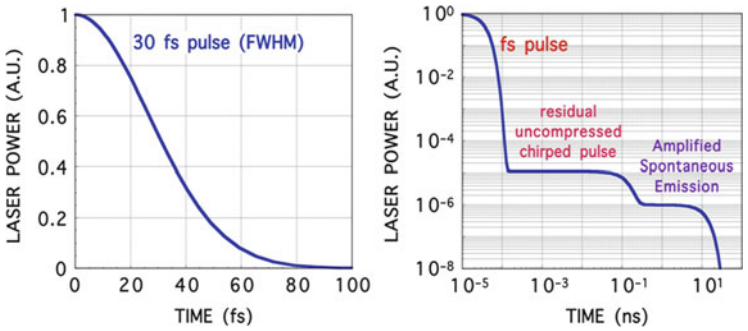

Fig. 10.3 Schematic profile of laser pulse power on a linear scale (*left*). The same laser pulse temporal profile plotted on a log scale (*right*) shows low power features due to amplified spontaneous emission in the amplifier chain and spurious light due to imperfections in the optical compression. These components, depending on the experimental configuration, can give rise to premature plasma formation on the target with a consequent change of interaction conditions

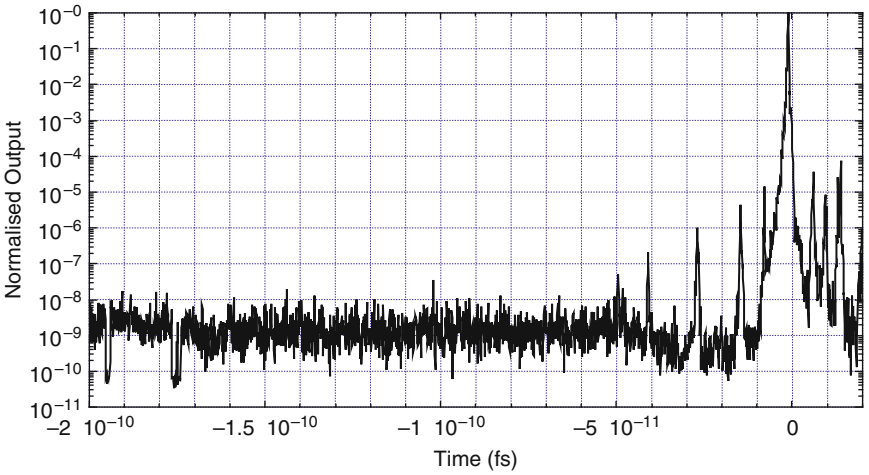

Fig. 10.4 Laser pulse contrast measurement obtained from third-order cross-correlation trace of the ILIL FIXER laser pulse after a two-stage amplification (10 mJ). Measurement by Amplitude Tech using a *SEQUOIA* cross-correlator

a two-pass amplifier that works in a relatively low-gain (3X) regime. According to this profile, the FIXER laser system has a contrast between 10^8 and 10^9.

The cross-correlation trace also shows low-intensity short pulses preceding the main pulse. These pulses are unlikely to play a crucial role in the interaction, even in the case of solid targets, because of their short duration that, in the worst case, will lead to generation of a very small, cold plasma. Clearly visible in the plot is the main pulse appearing at about time zero, followed by post pulses.

To study the effect of such complex structure of femtosecond pulse profiles, experiments have been performed using thin plastic foils as targets. A range of experiments performed in the past two decades used this technique for generating test plasmas with long-scale-length plasmas. In fact, when the laser intensity on a foil target is higher than the damage threshold of the foil, the foil explodes and is then heated by the laser radiation. This method was used to create conditions that are similar [5] to ICF coronal plasmas where the fuel *pelle*t is heated and a plasma is created all around. The use of exploding-foil targets was found to be effective to achieve coronal-like plasmas for laser–plasma coupling studies. In the case of irradiation by long pulses, a simple analytical model [6] can be used to obtain the expected values of density and temperature scale lengths of these plasmas in a self-similar expansion model. Alternatively, numerical codes [7,8] can be used to obtain full description of the expected hydrodynamics of the plasma produced by laser irradiation of such foils.

In the case of irradiation with femtosecond CPA pulses, thin foil plastic targets have peculiar properties owing to their higher damage threshold (in comparison with metallic targets) and remain therefore undamaged up to relatively high intensities, typically between 10^{11} and 10^{12} W/cm^2.

Since thin plastic foils are optically transparent, if the laser intensity is increased starting from well below the damage threshold, the electric field of the electromagnetic (e.m.) wave will be allowed inside the target. Thus, interaction with the volume of the target (rather than with the surface) will take place. In general, if the intensity of ASE on target is below the damage threshold for the thin foil, one may have a condition in which no precursor plasma is generated and interaction of the main pulse with a steep density gradient on the target may be achieved. When preplasma free conditions have been achieved at very high peak intensity, anomalous propagation effects have been observed showing unexpectedly high transmissivity and large ionization blue shift [9]. Absorption of the laser energy by the target will occur mainly at the critical density due to resonance absorption or the Brunel effect [10] and fast electrons will be generated directly or by the collision-less dumping of the resonantly excited electron plasma waves. As discussed below, these circumstances can be verified by investigating the polarization dependence of secondary radiation like X-rays and/or laser harmonics [11].

In contrast, at sufficiently high ASE levels, the thin foil will be exploded by the ASE prior to the arrival of the main pulse. In these circumstances, the above-cited analytical and numerical models can be used to estimate the conditions of the precursor plasma generated by the ASE, so that CPA pulses interact with known plasma conditions. A similar scheme has been used to successfully perform laser–plasma electron acceleration experiments [12].

In the following we present a few examples of the use of thin foils and how to diagnose the interactions. The first is a simple experiment in which a femtosecond laser pulse is focused on the target and X-ray and optical emission is detected to characterize the interaction in different linear polarization conditions. In fact, if the interaction does not suffer from excessive precursor plasma, then the pulse can reach the critical density. In this case, the absorption mechanisms, which are expected to

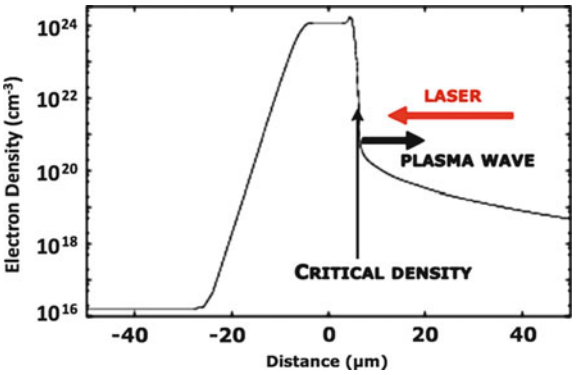

Fig. 10.5 Typical density profile of a plasma produced by interaction of an intense, short pulse with a solid target, for a relatively low level of ASE precursor radiation. A key role is played by the critical density layer where laser absorption takes place

take place, will be polarization dependent. Indeed, the experiment [11] shows that a strong dependence on the polarization is observed by looking at both the X-ray emission and the second harmonic emission from the specular reflection direction. These measurements show that polarization studies provide an effective method to identify the interaction mechanisms. On the other hand, when femtosecond laser target interactions are used as X-ray sources [13] this method can possibly be used to control the intensity of X-rays.

A possible scenario for the observed results is that energy absorption is dominated by resonant [14] or not-so resonant absorption [10] as schematically described in Fig. 10.5. Here we assume a relatively steep profile because of the expected low level of ASE. Therefore, the plasma is generated either by the CPA pulse itself or by picosecond-level prepulses shown in Fig. 10.3 (right). In either case, the gradient will have a scale length of the order of a micrometer or less. If the incident laser light is p-polarized, i.e., with the electric field in the plane of incidence, then at the turning point the electric field points in the direction of the density gradient in the target. In this way the laser field resonantly excite electron plasma waves at the laser frequency [14]. Then the plasma waves undergo noncollisional damping processes, thereby generating the so-called *fast electrons*, i.e., a population of electrons with an energy significantly higher than the energy of the electrons in the rest of the plasma. These *fast* electrons were observed many years ago in quite different experimental conditions as described in [15] (and references therein) and are now gaining importance, due to their potential role in the ICF FI scheme [1].

If metal targets are used instead of plastic (dielectric) targets, than even low levels of ASE can generate a large preplasma that can change the interaction conditions, making collisional absorption more effective [14].

However, at sufficiently high intensities, collisional absorption is suppressed due to the high velocity of electrons quivering in the laser electric field [14]. In these circumstances, even though there is a large plasma in front of the target, little energy of the laser is transferred to the plasma until the laser radiation reaches the critical density. Hence, the critical density is reached and the dependence on the polarization

can still be observed. This is not the case when a long pulse or a low-intensity short pulse with the precursor plasma are used.

Relatively thick targets are instead used for the generation of Kα radiation as an X-ray sources for applications [13] and for the study of fast electron transport [16]. The basic idea here is to focus intense ultrashort laser pulses on a solid targets to generate fast electrons as described above. These fast electrons propagate through the cold target substrate and generate fluorescence Kα radiation that escapes from the target. For an efficient production of Kα radiation, the target thickness is large compared to the interaction processes, but is comparable with or smaller than the range of the fast electrons. In fact, the requirement for an efficient, short pulse emission of Kα radiation is that electrons release the maximum possible energy in the target and at the same time Kα radiation can escape from the target.

Also, in order to keep the duration of the Kα emission as short as possible, the extension of the Kα emitting region should be small to limit collection of radiation from regions where multiple scattering of electrons takes place, which would increase the duration of X-ray emission. Hence, the thickness of the target should be carefully matched to preserve the quality of the output X-ray pulse. Since the early works on Kα sources [13], an extensive cross-disciplinary literature is available demonstrating that laser-driven Kα sources are now commonly used for applications in which short and ultrashort pulses are needed [17–21].

As discussed above, laser radiation may still reach the critical density provided its intensity exceeds $10^{17}\,\mathrm{W/cm^2}$ for one micron wavelength, which is the limit for suppression of collisional absorption due to nonlinear effects. Under these conditions, half-integer harmonic emission occurs as one of the signature features of this regime. This emission originates from propagation of the laser light in the long-scale-length plasma at the quarter critical density region where either two-plasmon decay [22] or Raman instability [23] can develop generating longitudinal electron plasma waves at half of the laser frequency. Nonlinear coupling of these plasma oscillations with the e.m. wave of the laser at the fundamental laser frequency generates the 3/2 harmonic emission. If the critical density layer is reached, second harmonic emission can still take place, mainly in the direction of specular reflection, provided that the critical density surface is not significantly distorted. From an experimental viewpoint, the scattering of optical radiation in the specular direction can be used to monitor the interaction in order to locate the regions where the most effective laser–plasma coupling takes place.

An example of optical scattering for the $(3/2)\omega$ emission is shown in Fig. 10.6. This data was taken using the femtosecond laser system of the Laboratoire d'Optique Appliquée (LOA) (in Palaiseau, France). Here, the optical spectrum was obtained by collecting the radiation emitted in the specular direction, and by spatially resolving it in the direction perpendicular to the spectral dispersion axis. Space resolved spectra like this can be used to identify the quarter critical density layer, provided that electron plasma waves generated by SRS or TPD couple with the laser field before significant propagation takes place [24]. An important conclusion of the entire experiment in which this measurement was taken was that the emission at $(3/2)\omega$ was strongly correlated with the presence of a large preplasma. In other

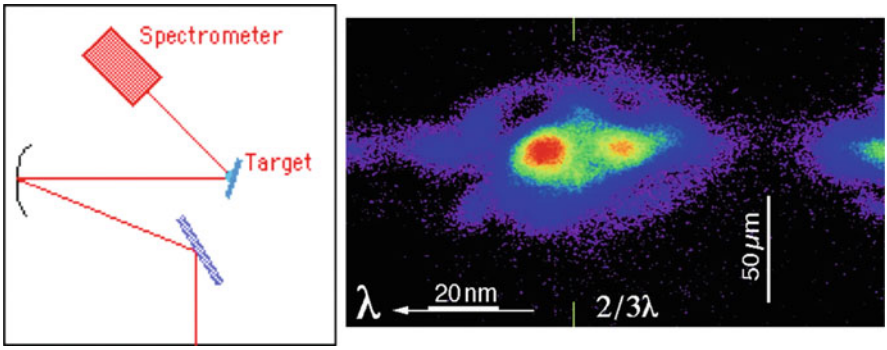

Fig. 10.6 Space resolved spectrum of specular $(3/2)\omega$ emission from the interaction of a 35 fs laser pulse at an intensity of $10^{19}\,\mathrm{W/cm^2}$ with a 1-μm thick plastic target. The intensity of the ASE was $10^{12}\,\mathrm{W/cm^2}$, i.e., sufficiently high to lead to premature plasma formation. The spectrum shows a very broad emission that is spatially localized on the position of the laser spot on target. Both *red* and *blue* components are present

words, this emission could be used as a marker of premature plasma formation by the ASE.

In the case of 2ω, a similar situation takes place. In this case, the emission originates from the critical density layer and the structure of the emission can be used to diagnose the interaction and to detect where the interaction is generated and what are the main mechanism for the energy exchange between the laser and the plasma wave.

An example of emission at 2ω is shown in Fig. 10.7, where a space-resolved spectrum of specular emission is displayed. The spectrum shows complementary blue and red shifted components where the shift is likely to originate from a combination of propagation and ionization effects. We also observe that the pattern shown in Fig. 10.7 is not reproducible from shot to shot, indicating that the regions from which the emission originates change. This variability may also depends on the laser beam stability and quality. In fact, if hot spots are present in the laser focal spot, some of these hot spots may activate emission.

In the general case of laser interaction with solids, when second harmonic emission occurs, in general it is generated by interaction at the critical density region. Another example of this emission is given in the plot of Fig. 10.8. It shows the emission from the interaction of the JETI laser system at the Institute of Optics and Quantum Electronics (IOQ) (Jena, Germany) with a 12- μm thick titanium foil. The laser pulse in this case was 60 fs FWHM and the intensity was $10^{19}\,\mathrm{W/cm^2}$. Visible in the spectrum of Fig. 10.8 are both the 2ω and the $(3/2)\omega$ emission indicating nonlinear coupling of the laser light at the critical density layer as well as with electron plasma waves at $\omega/2$.

A much similar situation is found also when significantly longer laser pulses are used. The plot of Fig. 10.9 shows the spectrum obtained from interaction of a 500-fs laser pulse using the TITAN laser at the Lawrence Livermore National Laboratory.

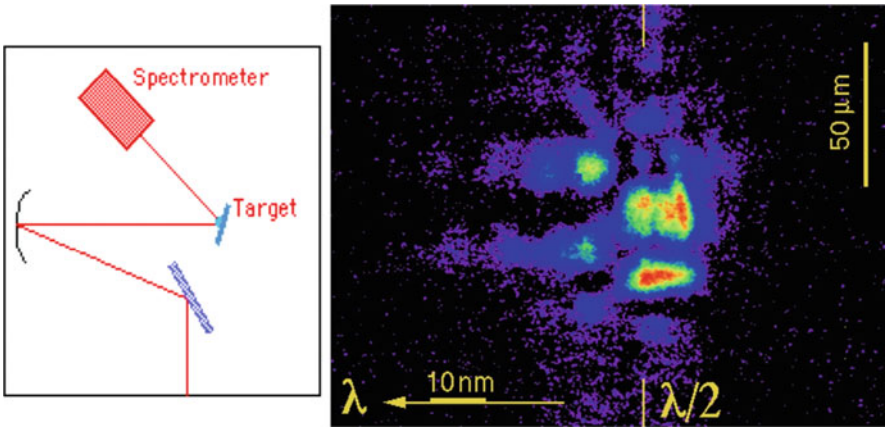

Fig. 10.7 Space-resolved spectrum of specular 2ω emission from the interaction of a 35 fs laser pulse at an intensity of 5×10^{18} W/cm^2 with a 1-µm thick plastic target. The intensity of the ASE was 10^{12} W/cm^2, i.e., sufficiently high to lead to premature plasma formation. The spectrum shows a very broad (spectrally) and large (spatially) emission with complementary red- and blue-shifted components

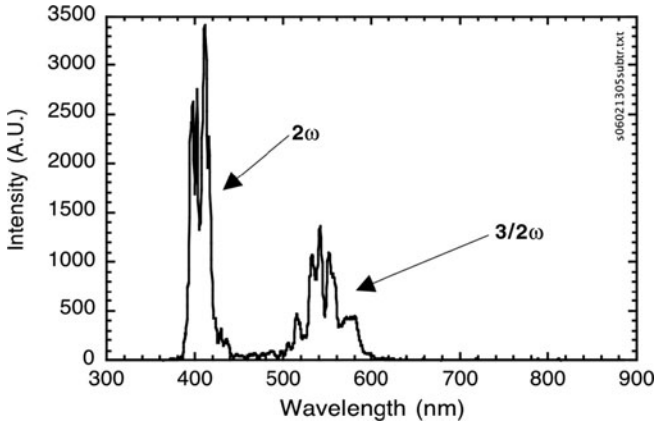

Fig. 10.8 Spectrum of optical scattering from laser interaction of a 60 fs laser pulse at an intensity of 10^{19} W/cm^2 with a 12-µm thick solid target. The spectrum was taken with a spectrometer capable of resolving the entire visible range, showing simultaneously the 2ω and the $(3/2)\omega$ emission components

In this case, a solid steel target was irradiated at an intensity exceeding 10^{19} W/cm^2. Clearly visible in the spectra are the second harmonic and $(3/2)\omega$ emissions. In this case, the $5/2\omega$ emission is also visible, indicating a stronger nonlinear coupling of the laser e.m. field with the plasma waves.

Additional measurements performed with the same experimental also show that the second harmonic emission spectrum obtained from the steel target is broader

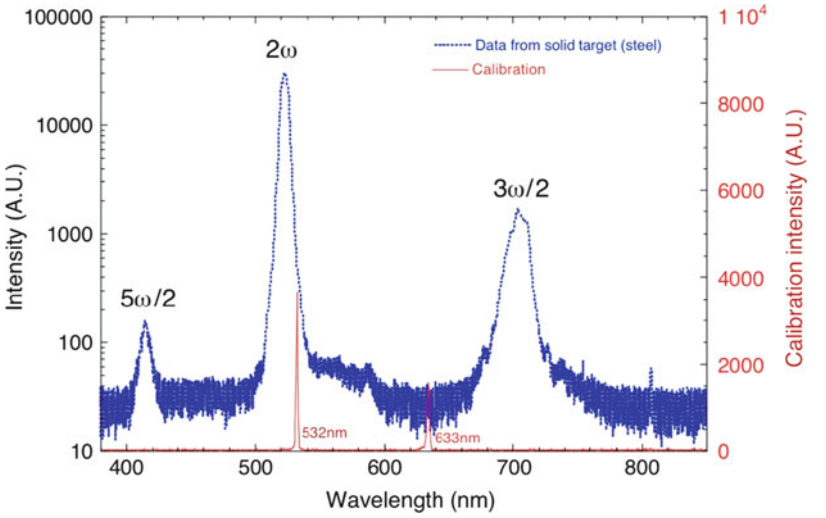

Fig. 10.9 Spectrum of the radiation emitted from interaction of a 500-fs laser pulse at 10^{19} W/cm^2 with a solid (steel) target. The spectrometer was set to detect the radiation emitted in the specular direction

than the similar spectrum obtained from irradiation of a plastic target suggesting that stronger spectral modifications of the laser radiation occur in the case of the steel target, while propagating towards the critical density layer. In this case, due to the fact that metal targets are more sensitive to the precursor radiation, longer-scale-length plasmas are generated compared to dielectric plastic targets. Therefore, in the case of metals, the laser light has to propagate over a longer plasma before reaching the critical density layer, thus undergoing stronger spectral modifications, possibly due to ionization. Although deconvolution of this information is not straightforward without a detailed modeling of propagation and ionization, it can be immediately used to provide a qualitative assessment of the regime of interaction occurring in a given experimental configuration. In particular, the use of this technique is highly recommended to monitor the interaction in experiments in which solid targets are used to activate Kα generation [25,26]. In these circumstances, optical spectroscopy of the scattered radiation from the target (e.g., in the reflection direction) can be used as an monitor for the control of laser–target interaction for Kα sources, to stabilize the source intensity.

An example of a possible drift of long term behavior of the second harmonic and $(3/2)\omega$ emissions in laser–target interaction for Kα generation is shown in Fig. 10.10 where the spectra obtained from a sequence of 800 shots obtained in similar conditions as in the spectrum of Fig. 10.8 is shown. The image consists of a sequence of individual spectra displayed as 1D false color images placed next to each other to form a single image. The sequence was sorted from left to right according to the increasing order of the corresponding yield of X-ray emission, including Kα fluorescence, as measured from a separate CCD detector. The plot

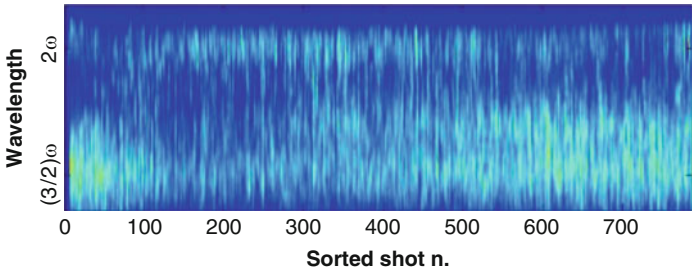

Fig. 10.10 Multi-shot spectra of optical emission from laser interaction of a 60 fs laser pulse at an intensity of $10^{19}\,\mathrm{W/cm^2}$ with a 12-μm thick solid target. The image consists of a sequence of spectra as that of Fig. 10.9, displayed as a false color image. The sequence is sorted from left to right according to increasing yield of X-rays as measured from a separate detector

shows that there is a region of high $(3/2)\omega$ emission corresponding to low X-ray emission yield. As the X-ray yield increases, optical emission is characterized by a weaker $(3/2)\omega$ emission and a brighter 2ω emission. Finally, at higher X-ray yield, lower 2ω emission and brighter $(3/2)\omega$ emission occur, with the $(3/2)\omega$ showing a broadened and spectrally modulated emission.

A possible explanation of the behavior at higher X-ray yield is that a strong interaction occurs in the lower-density plasma region, reducing the laser energy that reaches the critical density. Hence, efficient coupling occurs at the quarter critical density, likely producing higher-energy electrons as discussed above. These high-energy electrons escape and pass through the target producing *Bremsstrahlung* emission with little Kα emission. In contrast, the high second harmonic emission occurring for the shot number range from 150 to 500 suggests that more efficient coupling occurs at the critical density region, and the condition becomes more relevant to efficient generation of Kα X-rays. In summary, these measurements show simple spectroscopic measurements can be used to monitor, and, possibly, control laser–plasma X-ray sources.

10.2 Optical Interferometry and Propagation Issues

If the temporal evolution and detailed spatial features of the plasma have to be investigated during propagation, additional techniques like plasma probing should be used. In fact, there are several reasons for studying the propagation of intense laser pulses in gases and most of them are related to the laser acceleration of electrons in gas-jets [27] or in capillaries for which energy up to the GeV range has already been demonstrated [28]. However, there are still significant concerns for the stability and reproducibility of the main parameters of the accelerated electron bunches. Recent experiments based upon counter-propagating laser pulses have shown that some control of the electron bunch energy can be achieved [29]. However, it is clear

that reproducibility and stability are strictly related to laser propagation issues and a lot remains to be investigated.

Presently, a significant effort is being made worldwide to establish the technique from the viewpoint of the high-energy physics (HEP) community, presently facing difficulties due to the gigantism of conventional accelerators. However, the need of the HEP community is focused on reliable ways of accelerating particles with high-quality parameters, including very small energy spread. In order to generate interest from that viewpoint, the laser–plasma acceleration technique must establish itself in terms of quality and stability. This is the focus of the effort of many groups worldwide. In Italy, the laser–plasma acceleration community and the HEP community are now entering this arena with an entirely new project [30–32] based upon the FLAME laser [27], a 20-fs, 300-TW Ti:Sa 10-Hz system specifically designed to investigate the full potential of laser-driven acceleration.

To illustrate the basic issues in laser–plasma acceleration, in the following we explore a series of experiments aimed at studying propagation of an ultra-intense laser pulse in a gas-jet using optical probing and interferometry. The techniques are the same used in the past to diagnose plasmas produced by long laser pulses. However, special attention is dedicated here to highlight new effects arising from the use of ultrashort pulses to probe plasmas. In fact, several issues arise including ionization front smoothing due to finite probe pulse transit time [33] and loss of fringe visibility [34].

The basic experimental setup for the study of laser propagation in a gas is shown in Fig. 10.11. In this set up the laser pulse is focused on a target consisting of a gas-jet capable of producing a slab of gas with steep edges and peak density exceeding 10^{19} el/cm^3. The probe pulse propagates along the direction perpendicular to the propagation direction of the main laser pulse to detect changes of refractive index induced by ionization.

Figure 10.11 also shows the phase shift map of a He gas-jet. The image shows a positive phase shift due to the small refractive index of neutral He atoms. As

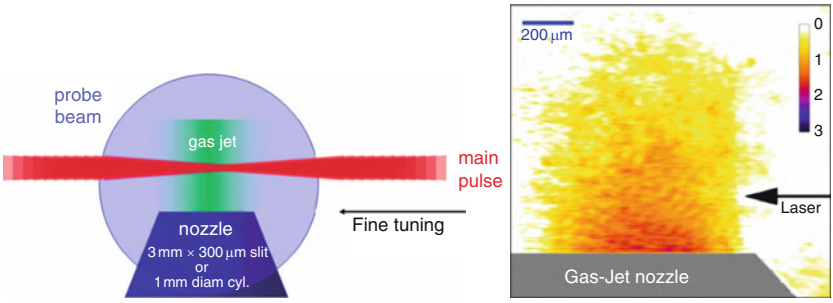

Fig. 10.11 Typical schematic experimental setup for study of propagation of an intense ultrashort laser pulse in a gas-jet target. The focal spot position can be moved relative to the gas-jet and the probe beam (*gray circle*) is set to propagate perpendicular to the main laser pulse. Also visible on the right is the map of the phase shift induced by neutral helium gas on the probe pulse as measured by the interferometer

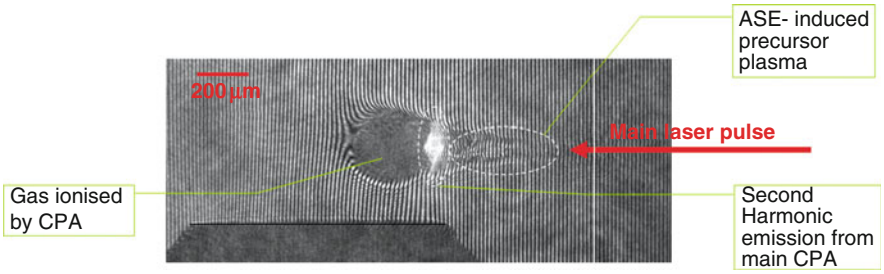

Fig. 10.12 Interferogram of the laser–plasma interaction region in a gas-jet experiment as that schematically shown in Fig. 10.11. The interferogram was taken with a short pulse probe timed to reach the interaction region 5 ps after propagation of the main pulse

discussed in [5], numerical techniques are used for the fringe pattern analysis to extract the small phase-shift information that was of the order of a small fraction of wavelength. The pattern is noisy because of the numerical noise, however, the shape of the gas-jet is clearly visible.

Figure 10.12 shows an interferogram taken 5 ps after the arrival of the main laser pulse on the gas-jet. Clearly visible is the effect of a short pulse propagating in the gas. It also shows the effect of the ASE that, in this case, gives rise to premature gas breakdown with a shockwave propagating radially as visible on the right-hand side of the image. This premature plasma formation is the reason why ASE is regarded as one of the sources of nonreproducibility of the interaction due to its strong level fluctuations from shot to shot. Because of this, several techniques are being implemented to reduce the level of ASE. Also visible in the image is second harmonic emission. This emission is due to a different mechanism [35] than the specular second harmonic emission from the critical density layer discussed above since the former is being observed at 90°. Finally, in the left-hand side of the image of Fig. 10.12, a third region is visible in which the laser has ionized the medium and this plasma region is opaque to the probe radiation, hence, no fringes are visible.

Under these conditions, electrons are still accelerated as shown in Fig. 10.13, but acceleration conditions are strongly affected by the presence of the ASE precursor plasma that prevents the main pulse to be properly focused due to uncontrolled refraction and defocusing effect. Measurements of accelerated electrons were performed using a technique [36] developed to detect the electrons and measure their energy. The technique uses a stack of layers of radiochromic films to measure the dose released by the electrons in the layers. By using some known stopping materials in between the layers, the energy of the incoming beam can be reconstructed. The angular distribution of these electrons can also be determined. In this case, a particular sequence of aluminum layers and radiochromic films was used as shown in the layout of Fig. 10.13. Actual raw data are reproduced in the figure, enhanced in terms of contrast for the purpose of displaying the shot-to-shot change. As one can see, strong fluctuations from shot to shot occur with the electron beam being produced by approximately only 30% of the shots. The initial plasma conditions

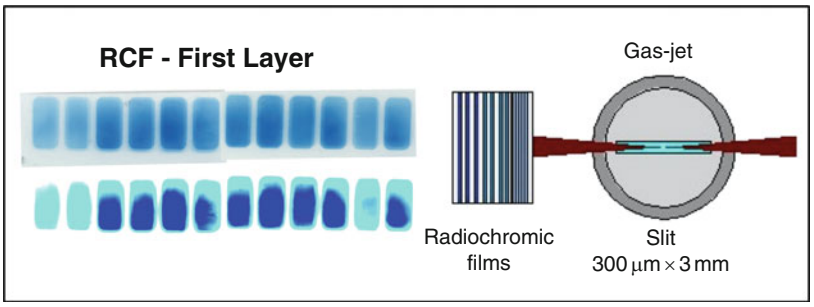

Fig. 10.13 Energetic electron production from a sequence of 12 laser interaction events with a gas-jet, in the presence of precursor plasma due to ASE. Measurement of angular and energy distribution using stack of radio chromic films show strong fluctuations from shot to shot

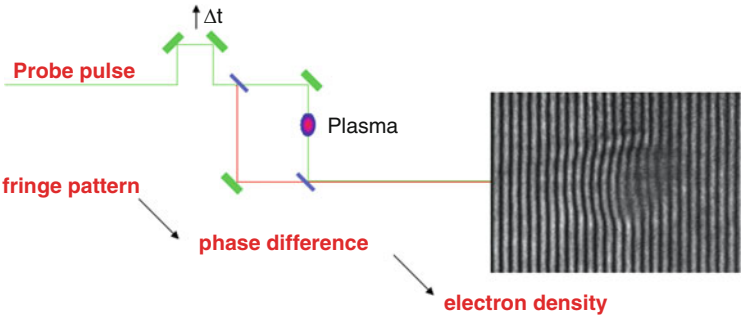

Fig. 10.14 Conceptual layout of a laser plasma interferometer showing the sequence of steps required to retrieve the map of electron density distribution from the detection of fringe shift induced by the plasma via its refractive index

(at the time of arrival of the main short pulse) are most likely the reasons for this behavior as displayed by plasma probing via interferometry.

As anticipated above, special attention requires the use of very short probe pulses in laser plasma interferometry. In view of this discussion, it is useful to recall the basic principles of plasma interferometry. Figure 10.14 shows a typical Michelson-type interferometer. The beam is split and the resulting two beams are made to interfere, after one of them has propagated through the plasma. Once the fringes are obtained, the phase difference can be retrieved and, by the deconvolution of the phase difference assuming a cylindrical symmetry, the electron density is finally obtained. A number of papers have been published on laser plasma interferometry and deconvolution techniques as discussed in [5], with the latest advances being in the use of wavelet transform, where a different technique is used to deconvolute the fringe pattern [37] as an alternative to the standard FFT technique. Special algorithms can also be used to account for a small degree of asymmetry in deconvolution [38].

If short pulses are used, then there are several limitations that should be taken into account when deconvolution is done. One is the probe transit time that occurs when the probe pulse is very short in comparison to the time taken by the probe-pulse to cross the evolving interaction region. A second limitation is related to the visibility of the fringes, which suffers from the usual losses well known [5] in the case of long pulse probing techniques, plus additional mechanisms of fringe visibility depletion due to fast evolution of the electron density due to fast ionisation.

To explain these circumstances we consider here a simple case in which the change of the refractive index is due to a glass cylinder moving in the field of view of our interferometer. This situation is somewhat similar to probing a very sharp change in the refractive index as we would expect from an intense short pulse propagating in a gas jet and generating a sharp ionization front. We consider the case of a short probe pulse with duration that is short compared to the time taken by the pulse to cross the cylinder, and the cylinder is moving while the probe pulse propagates through it. This motion limits the spatial resolution of the interferometry and, as a result, a sharp edge will be smeared out. In a similar way, if we probe the ionization front generated by an ultrashort pulse propagating in the gas, the longitudinal (along the laser propagation axis) extent of the ionization front will appear broader due to the probe transit time.

Figure 10.15 shows a typical situation in which an ionization front generated by a femtosecond laser pulse in a gas propagates from right to left. The fringes that are shifting and being displaced due to the change of refractive index in the laser ionized region. The displacement ranges from zero to the maximum. However, it is not sharp; any sharp change of the refractive index will be seen as a smooth change in the phase shift. This is a very complex problem and deconvolution is a rather difficult task. In some circumstances this analysis leads to the identification of picosecond prepulse effects as discussed in [39].

In terms of fringe visibility, the typical losses are due to absorption and refraction. Whenever a probe pulse propagates through the plasma, it will be either refracted or absorbed. Under this condition, one of the two beams that undergoes interference makes the fringe pattern disappear by decreasing its intensity and typically, the average intensity integrated over a period of the fringes is less than the average intensity of the unperturbed fringe pattern (without plasma). Fringe visibility is affected in this case and so are phase shift measurements.

There is another reason why the fringes disappear in the case of short pulses. In ultrashort interactions the changes in the refractive index are on a temporal scale that is fast compared to the probe pulse duration. Basically, if the plasma is changing while it is being probed, the instantaneous fringes will shift at the detector plane and this shift will appear as a loss of visibility due to the time integration of the detector recording the fringe pattern. An example is shown in the sequence of interferogram of Fig. 10.16 taken 1.34, 2.33, and 4.67 ps after arrival of the main pulse at the focal region, when the beam is out of the best focus region. As time goes and the main laser pulse propagates, ionization occurs and plasma is generated. The sudden ionization occurring at the leading edge of the laser pulse induces fringe motion and lower visibility. Behind this region, the density of the plasma is stationary (on the time scale of the probe pulse), and is relatively low, allowing the probe pulse

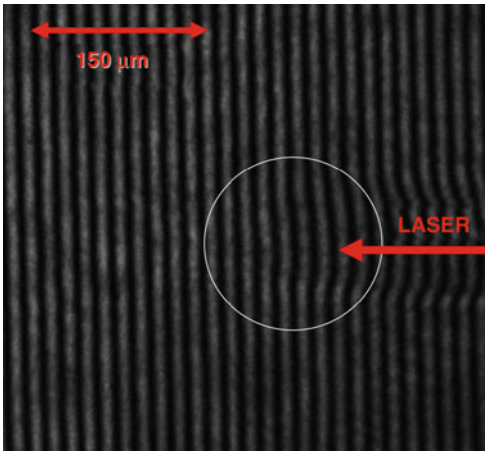

Fig. 10.15 Example of interferogram of ionization front propagating in a gas showing the smearing most likely due to the smoothing effect discussed in [39]. In this case a 30-fs laser pulse was propagating in a gas-jet at an intensity exceeding 10^{18} W/cm^2. The *circle* shows a smooth change of refractive index where a sharp transition is expected due to the ionization front

to propagate without significant absorption and the fringes are observed again. As indicated by the arrow, fringes are not visible in a region located at the leading front of the pulse.

A signature of this effect is that the average intensity of the region of the fringe pattern with low visibility becomes equal to the average intensity of the interfering pattern. This is the case for the middle interferogram of Fig. 10.16, where the intensity on the region of no fringe visibility is equal to the average intensity elsewhere. This simple estimate based upon a measurement of the average intensity allows us to distinguish between the different mechanisms of loss of fringe visibility driven either by refraction and absorption or by transient ionisation as in this case.

According to this mechanism, the speed of a fringe shift is basically given by the rate at which the density changes. A quantitative description of this has been developed [33] and according to this model, for a given density of the plasma and probe pulse duration and profile, the visibility can be estimated. For example, if there is a change of density of 2% of the critical density, a 100-fs pulse will produce a loss of fringe visibility of approximately 30%. This model has been used for a semiquantitative interpretation of experimental measurements of fringe visibility depletion [34] shown in the interferogram of Fig. 10.16.

In fact, a quantitative measurement of the loss in the fringe visibility can be obtained by using the same FFT analysis technique [40] for the extraction of the phase shift from the fringes. The whole analysis yields a complex result, the imaginary part gives the phase shift and the real part gives the fringe visibility. As a final result, the map of the fringe visibility is obtained in the range of 0–1. Figure 10.17 shows how the fringe visibility changes from frame-to-frame in a sequence obtained with a pump-and-probe like approach, i.e., by taking measurements with several shots at different probe pulse delay.

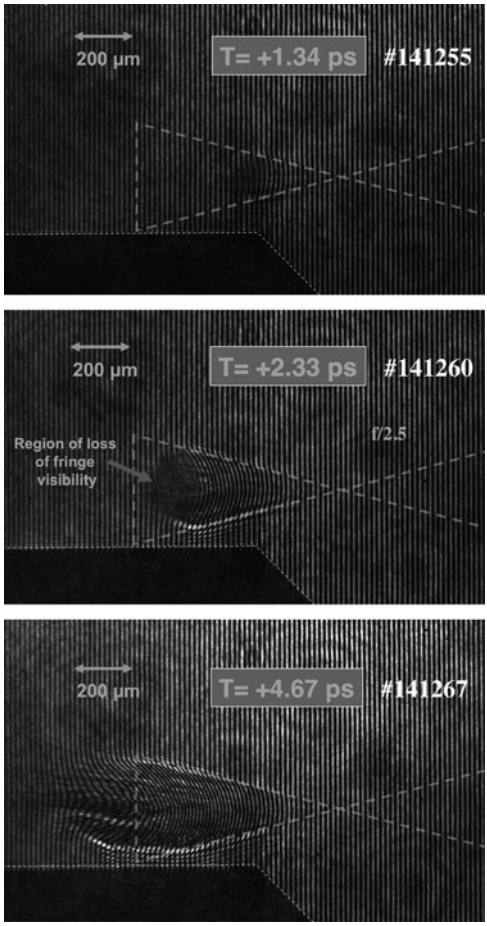

Fig. 10.16 Example of interferograms showing propagation of a laser pulse (from the *right*) in a gas. Partial loss of fringe visibility detected in the top interferogram becomes total in the middle interferogram, discussed in details in [34]. In this case a 30-fs laser pulse was used at an intensity of $5 \times 10^{18}\,\mathrm{W/cm^2}$. The *arrow* shows the region where total loss of fringe visibility occurs

This result was interpreted using the model discussed above to extract information concerning the longitudinal extent of the ionization front, that was found to be shorter than 70 μm. Here the measurement is limited by the relatively long pulse duration of the probe pulse (110 fs) as discussed in detail elsewhere [34].

10.3 Time-Resolved X-Ray Spectroscopy and Imaging

In this section we discuss X-ray-based diagnostics. First we show a few examples of conventional X-ray techniques used to investigate the basic physics of laser–plasma interaction. We start discussing time-resolved X-ray spectroscopy.

Figure 10.18 shows a typical set-up for X-ray spectroscopy in which we can clearly identify the basic components, the laser beam, the target and the detection

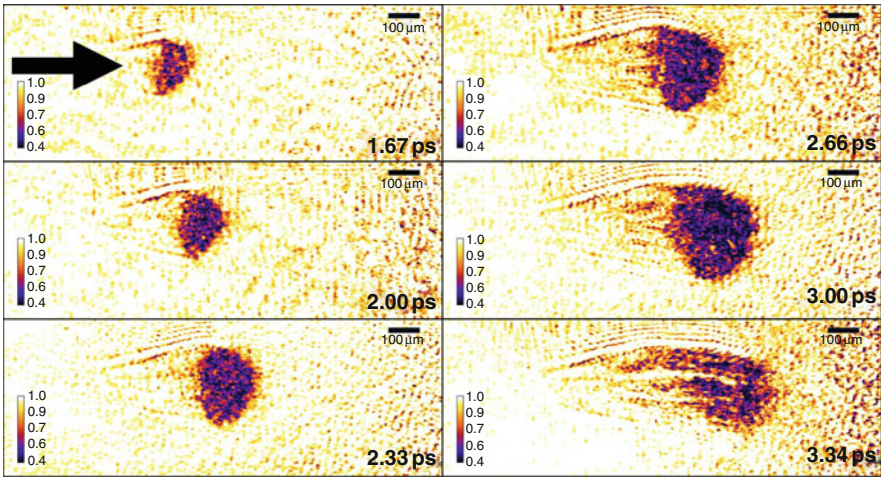

Fig. 10.17 Fringe visibility maps vs. time showing as the region where fringe visibility loss moves as the laser pulse propagates (from *left* to *right*)

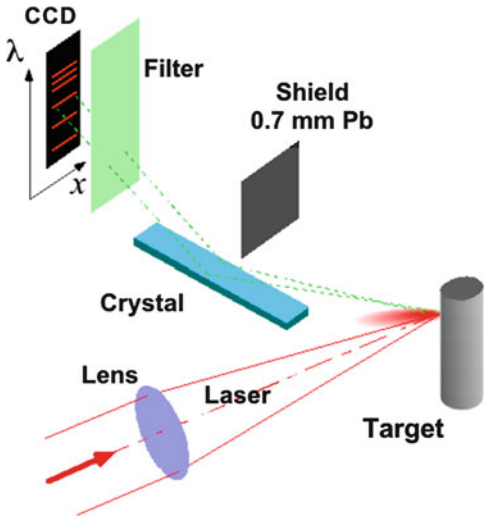

Fig. 10.18 Schematic setup for X-ray spectroscopy of laser-produced plasmas using a Bragg crystal as a dispersive element. Also shown in the image are the detector and the shield that prevents X-rays from the source to reach the detector directly. The filter is used to stop unwanted visible and UV light

system. A crystal with a known separation of the lattice planes is used to create Bragg-type diffraction. Because the source is very small, a spectrum is obtained whose resolution is limited by the source size [41].

Figure 10.19 shows a typical spectrum obtained using the setup of Fig. 10.18 from a plasma produced by laser irradiation of a solid Al target. In this case, a

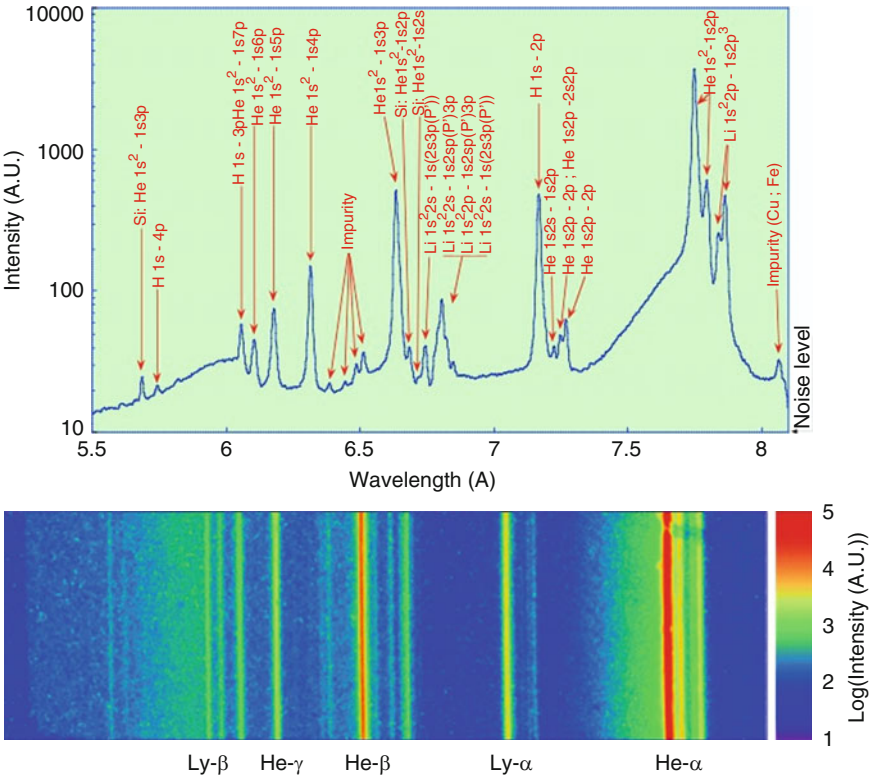

Fig. 10.19 Example of spectrum obtained using the setup of Fig. 10.18 from a plasma produced by laser irradiation of a solid Al target. Due to the small source size, the resolution is sufficiently high to allow identification of K-shell emission from helium-like and hydrogen-like aluminum

3-ns laser pulse from a Nd:YLF laser was used, focused to an intensity exceeding $10^{13}\,\mathrm{W/cm^2}$. In these experimental conditions, efficient transfer of laser energy to the plasma occurs and a hot plasma is generated leading to ionization of Aluminum up to the He-like and hydrogen-like configuration as demonstrated by the K-shell emission visible in the spectrum.

In order to unfold the temporal evolution of the plasma, temporal change in our spectra must be recorded on a very fast time scale, typically subnanosecond. The information thus obtained can then modeled using a combination of hydrodynamics and atomic physics modeling codes: the hydrodynamics provides the expected density distribution and atomic physics, the expected line intensity ratios. Then, these line intensity ratios are compared with the measured ones.

In the case of plasmas generated with long nanosecond pulses, the temporal resolution of the spectrum can be achieved by using an X-ray streak-camera to reach the temporal resolution below 10 ps. In the following, we described an experiment in which time-resolved X-ray spectroscopy is used to investigate the temporal

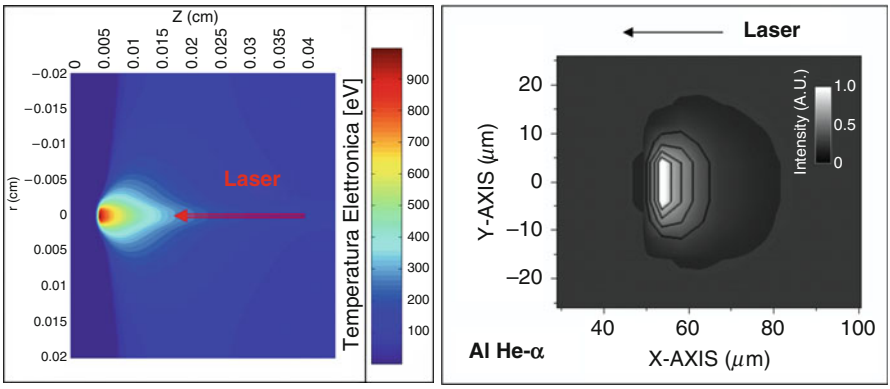

Fig. 10.20 (*left*) Map of the electron temperature of the plasma produced [43] by laser irradiation of a solid Al target at the peak of a 3-ns Gaussian laser pulse as predicted by POLLUX. The intensity on target was 1E14 W/cm^2, the pulse duration was 3-ns Gaussian and the laser focal spot was 8-μm FWHM. The target consisted of 50-μm thick Al. (*right*) X-ray emissivity at the He-α emission line calculated from electron density and temperature maps given by POLLUX using the code RATION/FLY

properties of X-ray emission in plasmas produced by nanosecond pulses [42]. In particular, the aim of the experiment was to identify, through time resolved X-ray spectroscopy, possible deviations of the plasma dynamics from the steady-state behavior during early stages of the interaction. The first step is the modeling of the interaction using the hydrodynamics code POLLUX [8] and we used the combination of RATION/FLY [42] and hydrodynamics results from POLLUX to calculate the expected emission in the spectral range of our diagnostics. The plot of Fig. 10.20 (left) shows the calculated electron temperature from the hydrodynamic calculations. This information, combined with the density map, is postprocessed using the code RATION/FLY to yield the expected emissivity at the required emission wavelengths. The plot of Fig. 10.20 (right) shows the result of this processing for a given time and a give emission wavelength in the form of a 2D map of emission.

Similar plots have been obtained [43, 44] for the entire emission time and for a set of emission lines. The ratio between α and β lines was then calculated taking into account the opacity effect that are expected to be significant for α lines. Figure 10.21 shows the final results in terms of comparison between measured and expected line intensity ratios for the steady-state and time-dependant models. The simulation predicts some changes in the nonstationary effect early in the pulse. After approximately 500 ps, the system becomes stationary. However, before that, there is a significant difference and the measurements were consistent with this separation. It should be stressed here that this effect could only be detected using temporal resolution.

In fact, since emission in the nonstationary regime only occurs early during the emission, its contribution would be largely overcome by the emission in the stationary regime and, therefore, be undetectable in time-integrated measurements.

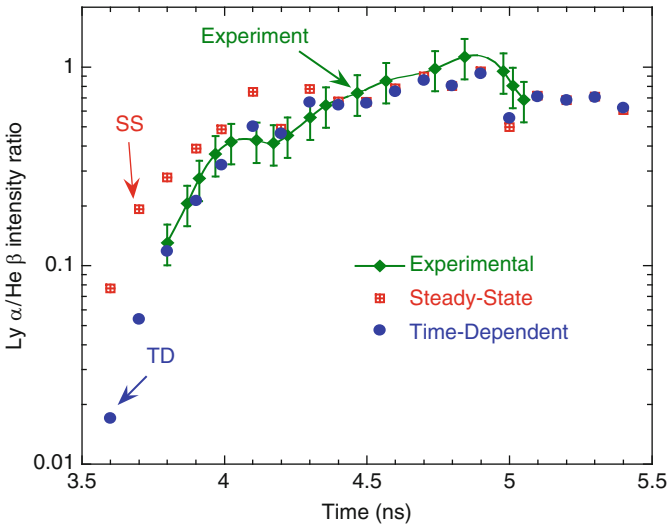

Fig. 10.21 Temporal evolution of Lyα to Heβ intensity ratio. Experiment vs. steady-state (SS) and time-dependent (TD) modeling

Figure 10.22 presents another experiment that shows the need of time-dependant X-ray spectroscopy. In this case, time-resolved spectroscopic techniques were used [45] to detect the cooling process of a plasma for different atomic species of the target.

The basic idea in this experiment was to measure the history of X-ray emission for plasmas produced by different elements and consequently infer information on radiation and cooling effects that may occur at a different rates depending on the plasma composition. Hence, it would be possible to probe the radiation cooling effects by using this X-ray spectroscopy. Figure 10.23 includes a comparison of time-resolved spectra of fluorine emissions from plasmas produced by irradiation of a range of targets containing fluorine, from the lighter LiF to the heavier SrF_2.

The analysis of the spectra of Fig. 10.23 shows that the temporal evolution of the electron temperature of this system depends on the charge state of the target. Indeed, the data show that this effect of radiation cooling plays an important role in these conditions ad discussed in details in [45].

Another interesting application of time-resolved spectroscopy concerns the study of electron transport measurements. A layered target was used and measurements were carried out to find the laser mass ablation rate, with a sufficiently short pulse that could separate the layers [46]. Targets consisting of thin layers of different materials were used to detect propagation of the heat front in the target as shown in Fig. 10.24 (left). According to hydrodynamics codes, the temperature of the first and third layers are expected to increase at different times as from the plots of Fig. 10.24 (right).

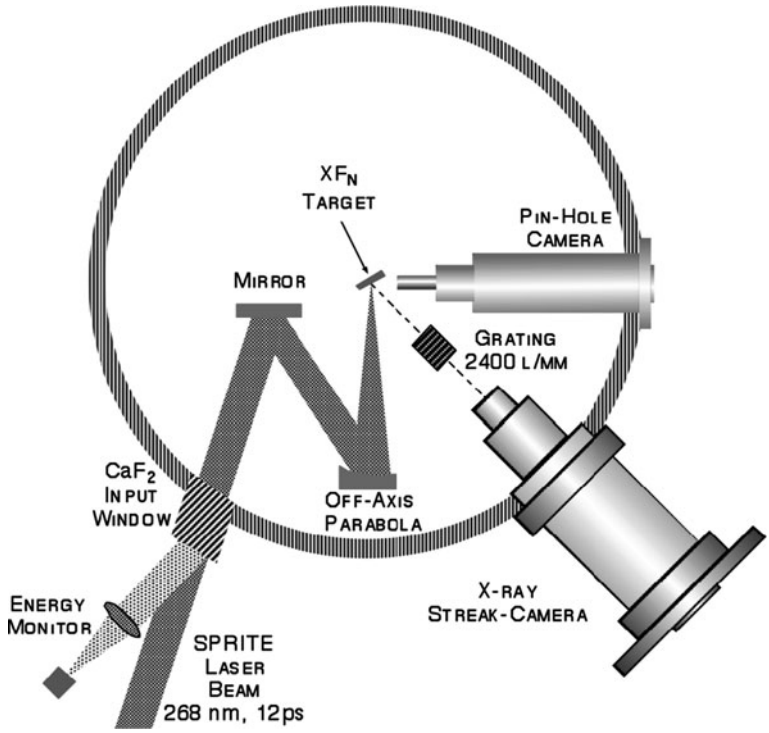

Fig. 10.22 Experimental setup of the interaction chamber for time-resolved soft-X-ray spectroscopy of picosecond plasmas [45]. The plasma was generated by the interaction of a high-contrast, 12-ps, 268-nm laser pulse with solid targets consisting of fluorine salts. The laser beam was focused on the target by means of an off-axis parabola at an intensity of $10^{15}\,\mathrm{W/cm^2}$ in a 30-μm diameter focal spot

Thus, if the X-ray emission from these layers occurs at different times, quantitative information on the transport of energy through materials is retrieved. Time-resolved measurements of X-ray emission from each of the layers was detected using characteristic line emission as shown in Fig. 10.25, which shows carbon emission from the first and third layers.

This measurement provide invaluable experimental data on the mass ablation rate that is used to investigate the flux limiter parameter in the heat propagation that takes place at a higher intensity as discussed in details in [46].

10.4 Fast Electron Production and Characterization

This section is devoted to fast electron propagation and to the description of novel experimental techniques of X-ray imaging having simultaneously micrometer special resolution and spectral resolution in the range of 1–10 keV. The motivation here

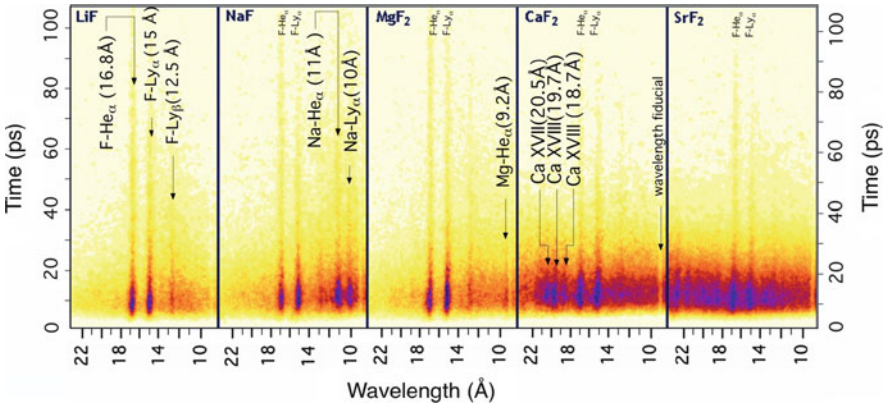

Fig. 10.23 Time-resolved spectra of the X-ray emission from LiF (*left*) to SrF2 (*right*), in the range from 10 to 22 Å, obtained with a spectrometer equipped with a flat-field grazing incidence grating (from [45]). The spectral and temporal resolution were 500 mÅ and 6 ps, respectively. Strong emission from bound–bound and free–bound transitions in H-like and He-like ions is visible. Short-lived continuum emission is also visible as a background emission due to Bremsstrahlung and recombination

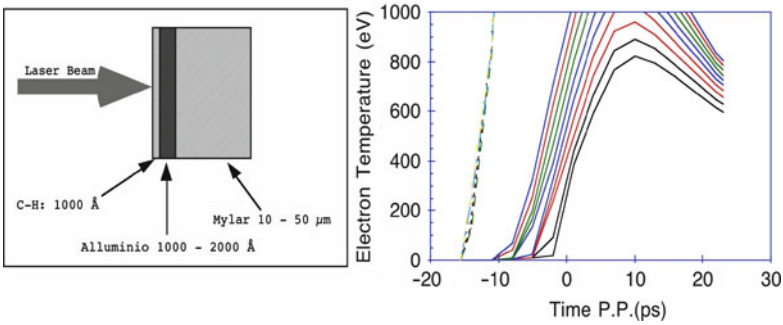

Fig. 10.24 (*left*) Target configuration for mass ablation rate measurements in intense laser–solid interactions [from [46]). The aluminum tracer layer is used to detect propagation of the ablation front. Numerical modeling (*right*) is used to calculate the expected evolution of the electron temperature to be compared with experimental measurements via time-resolved spectroscopy

is to understand how fast electrons propagate, how far they can get into the material, how much energy they have, and how much energy they release in the material. These studies are of a great relevance to the FI scheme of ICF as discussed in the introduction section.

There is no ideal experimental technique for this kind of measurements. There are instead several methods that can be used to retrieve pieces of information. Then, we need to use them together. In some cases optical probing can be used to image out the profile of the rear side of a laser irradiated foil target as described in [47]. Here measurements show the presence of a bump that is probably due to the effect of the fast electron currents.

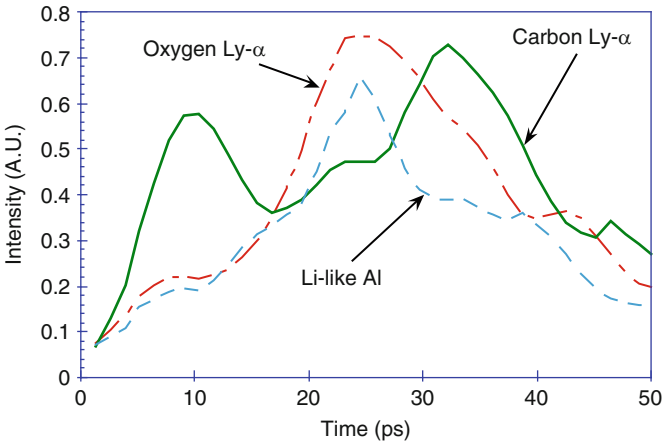

Fig. 10.25 Temporal evolution of X-UV emission line from irradiation of the target of Fig. 10.24 (*left*). Peak-to-peak delay in the H-like emission from C gives a measurement of the mass ablation rate in the Al layer. See [46]

In general, the most widely used techniques are based upon Kα fluorescence emission measurements with imaging and spectroscopy using flat and curved crystals. A new approach consists in the use a novel X-ray imaging technique with a micron-scale resolution and spectral resolution of ∼100 eV based on the use of multiple pin-hole imaging in the single photon (single-hit) detection regime.

Figure 10.26 summarizes the basic idea behind X-ray based techniques for the study of fast electron transport. Fast electrons that impact the cold atoms give rise to fluorescence emission. This process is described by curves like the one in this figure [48] that shows the fluorescence cross section as a function of the electron energy. According to this plot, the energy of electrons that we are most likely probed with fluorescence measurements ranges from a few keV to a few hundred keV. As shown in this plot, the cross-section peaks in the energy range between 10 and 100 keV. Similar behavior is found for different materials, making it possible to estimate the expected response of each target material to a given energy of the fast electrons. However, the fast electrons generated in ultra-intense laser interactions typically have a broad spectrum and fluorescence emission is generated from all electrons, up to energies of ∼10 MeV. Complementary measurements must therefore be performed to unfold the fast electron transport problem.

The use [49] of a single-hit detection technique on a *charge coupled device* (CCD) is based on a simple idea that was proposed around 15 years ago in X-ray astronomy and later applied to ultra-intense laser–plasma interactions [11]. Each X-ray photon impinging on the chip of a CCD produces a charge that is proportional to the energy of the photon. Provided the X-ray flux is sufficiently low, the charge induced by each photon can be measured and detected. The charge might be confined on a single pixel or might be spreading on several pixels depending on the energy of photons as well as on the depth of the CCD where the photon is absorbed.

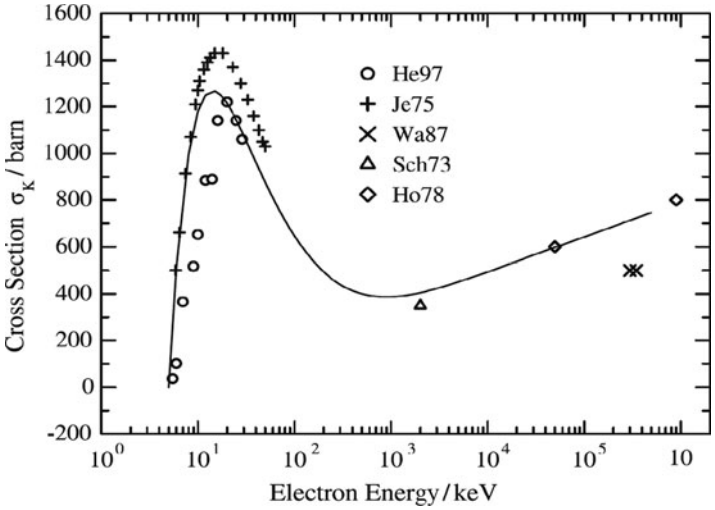

Fig. 10.26 Cross section of the fluorescence emission process in titanium (after [48]). The cross section has a pronounced peak between 10 and 100 keV. Above this value, the cross section decreases rapidly, reaching a minimum around 1 MeV and increases logarithmically for relativistic energies

For a given photon there are two different populations of "events" generated on the CCD: one is a single pixel and the other is a multipixel. Custom image processing techniques were developed to decouple the information and obtain the spectrum of the radiation [50]. Figure 10.27 shows a typical curve that gives the charge as a function of the energy of the photon incident on the CCD.

In the following we show the results of experiments in which this technique was applied to the measurement of the X-ray emission spectra from either single-layer of multilayer targets. In these experiments, single-hit measurement were carried out in a very noisy environment in which, typically, many photons and electrons scatter all around the area inside the vacuum chamber, generating a strong radiation background. To minimize the noise, several measures must be taken including the use of magnets to stop the electrons from streaming onto the CCD. In some circumstances it was also necessary to place the CCD outside the chamber to detect X-rays through a transparent window. Figure 10.28 shows a simple experimental set-up in which single-hit spectroscopy is used to study fluorescence emission from laser interaction with a titanium foil.

Figure 10.29 shows a typical spectrum obtained with the single-hit technique. As one can see from the plot, the technique allows the Kα emission to be easily resolved from the rest of the emission, as expected from the 90-eV resolution that was provided by the single-photon technique in our case.

The same technique shows its highest potential when dealing with multiple emission wavelengths as in the case of irradiation of multilayer targets. An experimental campaign was carried out at the JETI laser system at the IOQ in which the target

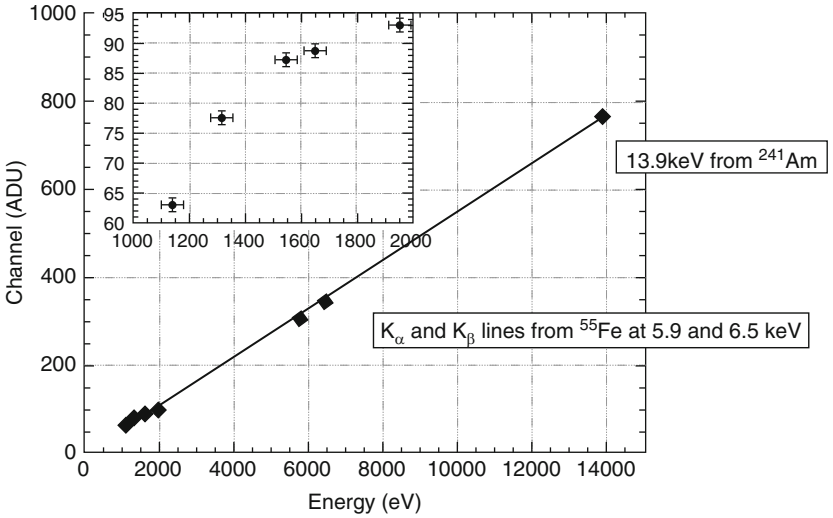

Fig. 10.27 Calibration of a CCD in the 1–14 keV energy range using a laser plasma X-ray source. The result of a linear fit of the points is also shown. In the inset a detail of the calibration points taken using the laser–plasma X-ray source is visible (after [50])

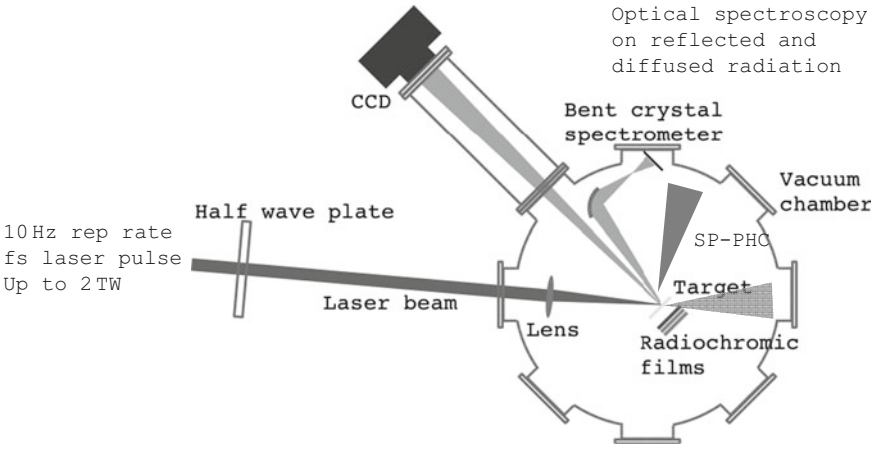

Fig. 10.28 A schematic experimental setup for the generation of fluorescence emission from interaction of intense femtosecond pulse of the ILIL FIXER laser system with a solid Ti target. The intensity on target was $2 \times 10^{17}\,\mathrm{W/cm^2}$ and the pulse duration was 67 fs

consisted of three layers of different metals characterized by different fluorescence emission wavelength and shown in Fig. 10.30. In addition to the spectroscopic measurements we also used a pin-hole camera equipped with a 5-μm diameter pinhole to obtain an image of the source [51]. The image is attenuated using filters, down to a level required by the single-hit detection. A sufficient number of images

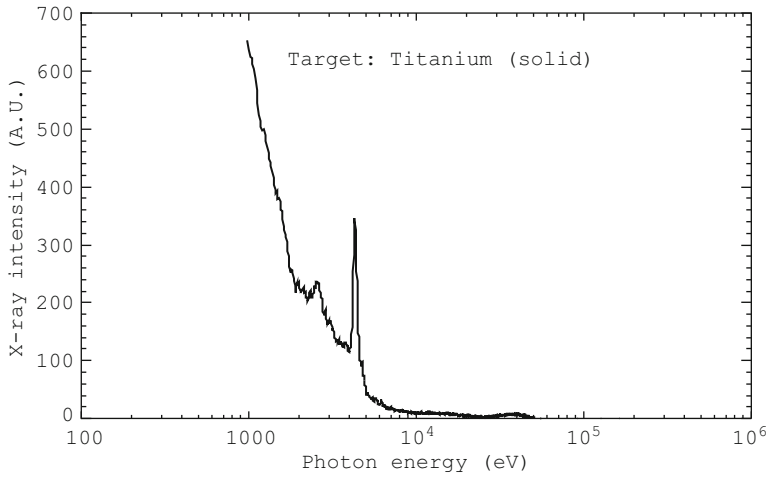

Fig. 10.29 Kα emission from titanium target irradiated with the Ti:Sa FIXER laser system of the ILIL lab, as measured using single hit spectroscopy with a CCD. The intensity of target was 2×10^{17} W/cm^2 and the laser pulse duration was 67 fs

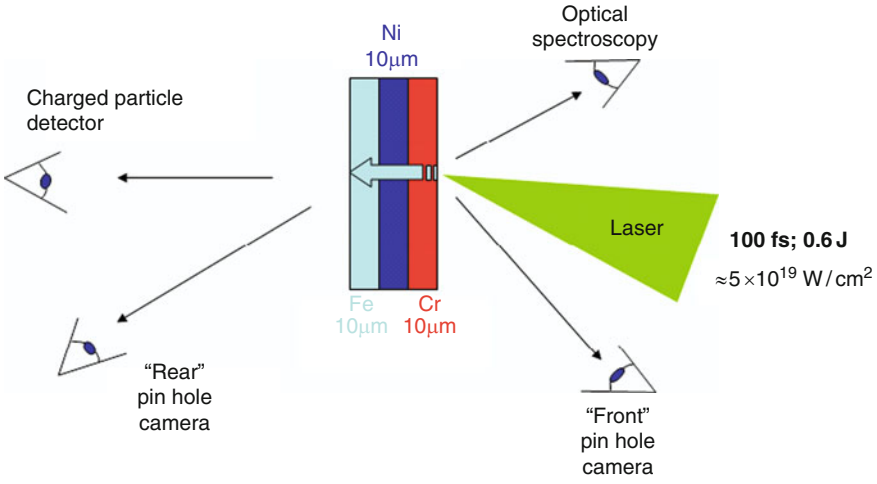

Fig. 10.30 Irradiation and detection setup for the experimental campaign on fast electron transport in solids carried out at using the JETI laser system. Imaging and spectroscopy based on single-hit detection of X-ray photons were implemented to recover full information on the production and transport for fast electrons

are captured resulting from respective laser shots, to obtain the number of photons required to build the full image at a given photon energy. In this configuration, the pin-hole camera acts as an energy-encoded imaging device (EEPHC) that can be used to obtain spectrally resolved images with 5-μm resolution.

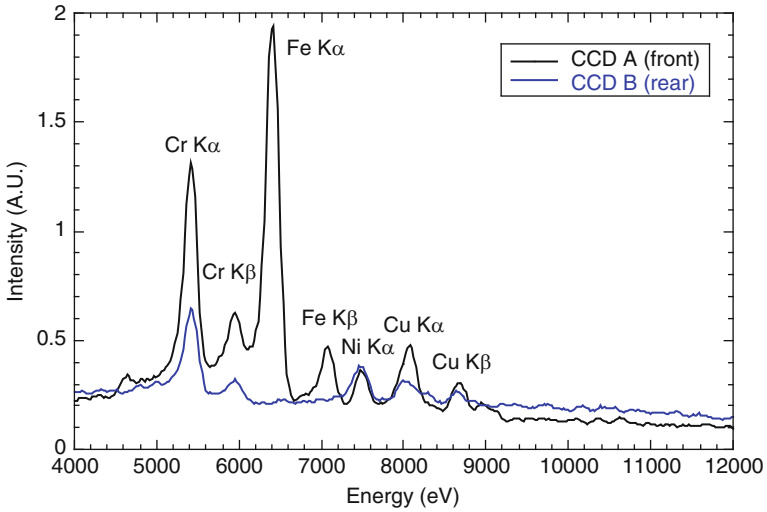

Fig. 10.31 Spectrum of the X-ray radiation detected from the front and the rear side of a three-layer Cr – Ni – Fe target of Fig. 10.30, irradiated at an intensity of 5×10^{19} W/cm^2. Note that the relative intensities of the two spectra are not to scale

Figure 10.31 shows the spectrum of the front and the rear side emission in which all the Kα lines from all the layers of the target can be identified. The spectrum was obtained adding up all identified photon from the analysis of the low flux images from 350 laser shots. The target was irradiated on the Cr side. The main Kα and Kβ line emissions from the Cr layer are clearly visible on the front and rear side images. The Ni Kα emission is also clearly visible from both sides of the target, while Fe Kα and Kβ are clearly visible only from the rear side.

Cu emission visible in both spectra is likely to arise from impurities in the Fe and Ni substrates. We observe here that the difference in the line intensity between the front and rear side spectra are also due to the filters and to the photon propagation and attenuation through the different layers. Therefore a quantitative analysis of these relative intensities will have to take into account this effect also. Measurement like this immediately shows that the electrons propagate through the three layers because the fluorescence emission peaks originating from all the three (cold) layers are identified.

Finally, energy-resolved images of the source at any given energy can be obtained by selecting the corresponding photons from the spectral distribution, by plotting them according to their landing position on the CCD detector and by taking into account the geometry of the pin-hole camera imaging system, including the magnification. Figure 10.32 shows the energy-resolved full imaging of the X-ray source at the Kα and Kβ line energy of the three materials, as seen by the front and rear side pin-hole cameras. In this case, a total of 1,600 single-shot images were used.

The upper side of Fig. 10.32 shows the images obtained selecting X-ray photons in an energy window around each Kα line (±230 eV). The lower side of the figure shows the images obtained selecting X-ray photons in a spectral region where no

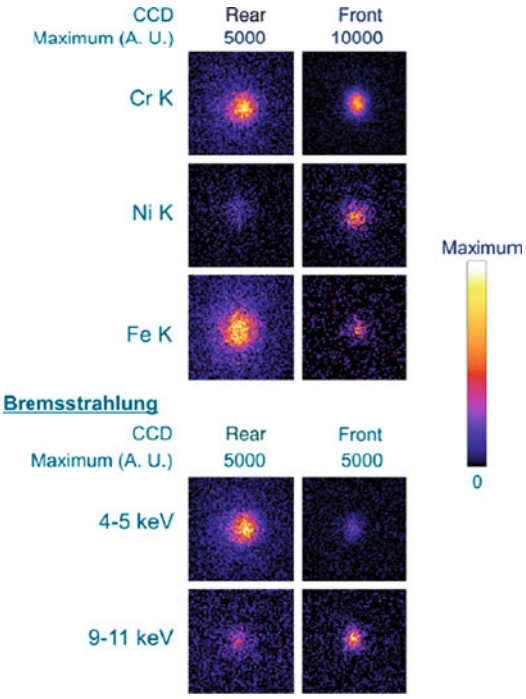

Fig. 10.32 Energy-resolved images of the Kα sources of Cr, Ni and Fe as seen from the rear (*left*) and the front of the target obtained selecting all the photons within a spectral window of ±230 eV. The lower part of the figure shows the images of the source obtained selecting the photons in two regions where no or weak line emission is expected to occur and where the main contribution is expected to be given by Bremsstrahlung emissions. The scale of the edge of each image window is 200 μm

spectral lines are expected, i.e., below the Cr−Kα and above the Ni−Kα. Therefore, contribution to these images is expected to come from continuum radiation, possibly arising from Bremsstrahlung emission.

Higher-energy photons are also present in the spectrum; however, for these energetic photons the 2.5-μm thick, pinhole Pt substrate starts becoming transparent and the contrast of the pinhole image consequently decreases.

From the spreading of electrons as visible fro the images of Fig. 10.32, the dynamics of propagation of the electrons can be inferred. This is a complex task that also requires a comparison with a detailed numerical modeling and additional information on the analysis of these data can be found elsewhere [51]. Here the potential of this diagnostic technique is outlined and how the experimental results can be used to clarify the fast electron propagation dynamics.

The technique "as it is" has currently a "multishot" basis due to the need for a statistically significant number of photons to be detected. The number of shots can be reduced by using a higher magnification, which would enable to collect a greater number of photons per shot, while satisfying the single-photon condition

on the CCD detector. Another possibility is to exploit large area CCDs or similar position sensitive devices in combination with a pin-hole array, to collect more than one "single-photon image" on the same CCD detector.

10.5 Summary and Future Instrumentation Requirements

In summary, an overview was given of experimental techniques for the investigation and characterization of laser–plasma interactions via description of a number of experimental studies carried out in the wide range of different experimental configurations. It was shown that spectroscopy of optical radiation scattered during the laser–solid interaction provides the detailed information on laser–plasma energy coupling mechanisms. Optical probing of laser interaction with gases with the femtosecond temporal resolution was shown to be sensitive to effects like the probe transit time and the fringe visibility depletion that are likely to affect measurements much more than in the case of long-pulse probing.

As for the application of X-ray spectroscopy and imaging, the potential of time-resolved spectroscopy in laser–plasma experiments was demonstrated even when using relatively long pulses to detect transient phenomena in the evolution of the plasma.

Finally, we described the latest development of a powerful X-ray investigation technique based on single X-ray photon measurements that promises to become a complete tool for imaging and spectroscopy in the X-ray range, ideal for FI relevant studies.

The experiments discussed here were also obtained through a number of collaboration experiments carried out at the Intense Laser Irradiation Laboratory at Istituto Nazionale di Ottica – CNR (Italy) and at several high-power laser facilities worldwide including the Central Laser Facility at STFC (UK), the JETI laser facility at IOQ, University of Jena (Germany), the SLIC facility at CEA (Saclay), the LOA at Ecole Polytechnique (Palaiseau), the TITAN laser at LLNL (USA). The main results of those experiments are the subject of several publications on international journals as pointed out throughout the text. The reader interested in expanding the topics presented here is encouraged to refer to those publications and references therein.

References

1. M. Tabak, J. Hammer, M.E. Glinsky, W.L. Kruer, S.C. Wilks, J. Woodworth, E.M. Campbell, M.D. Perry, R.J. Mason, Phys. Plasmas **1**, 1626 (1994)
2. S. Atzeni, J. Meyer-ter-Vehn, *The Physics of Inertial Fusion* (Oxford University Press, Oxford, 2004)
3. D. Giulietti, M. Galimberti, A. Giulietti, L.A. Gizzi, F. Balcou, A. Rousse, J.Ph. Rousseau, M.Borghesi, Phys. Rev. E **64**, 015402(R) (2001)
4. T. Ceccotti et al., Phys. Rev. Lett. **99**, 185002 (2007)

5. A. Gizzi, D. Giulietti, A. Giulietti, T. Afshar-Rad, V. Biancalana, P. Chessa, C. Danson, E. Schifano, S.M. Viana, O. Willi, Phys. Rev. E, **49**, 5628 (1994)
6. R.A. London, M. Rosen, Phys. Fluids **29**, 3813 (1986)
7. J.P. Christiansen, D.E.F.T. Ashby, K.V. Roberts, Comput. Phys. Commun. **7**, 271 (1974)
8. G.J. Pert, J. Comput. Phys. **43**, 111 (1981)
9. D. Giulietti, L.A. Gizzi, A. Giulietti, A. Macchi, D. Teychenné, P. Chessa, A. Rousse, G. Cheriaux, J.P. Chambaret, G. Darpentigny, Phys. Rev. Lett. **79**, 3194 (1997)
10. F. Brunel, Physical Review Letters **59**, 52 (1987)
11. L.A. Gizzi, D. Giulietti, A. Giulietti, P. Audebert, S. Bastiani, J.P. Geindre, A. Mysyrovicz, Phys. Rev. Lett. **76**, 2278 (1996)
12. D. Giulietti, M. Galimberti, A. Giulietti, L.A. Gizzi, P. Tomassini, M. Borghesi, V. Malka, S. Fritzler, M. Pittman, K. Taphouc, Letter on Phys. Plasmas **9**, 3655 (2002)
13. A. Rousse et al., Phys. Rev. E **50**, 2200 (1994)
14. W.L. Kruer, *The Physics of Laser-Plasma Interactions* (Addison-Wesley, New York, 1988)
15. L.A. Gizzi, D. Batani, V. Biancalana, A. Giulietti, D. Giulietti, Laser Part. Beams **10**, 65 (1992)
16. P. Köster, K. Akli, D. Batani, S. Baton, R.G. Evans, A. Giulietti, D. Giulietti, L.A. Gizzi, J.S. Green, M. Koenig, L. Labate, A. Morace, P. Norreys, F. Perez, J. Waugh, N. Woolsey, K.L. Lancaster, Plasma Phys. Control. Fusion **51**, 014007 (2009)
17. R. Neutze et al., Nature **406**, 752 (2000)
18. A. Rousse et al., Nature **410**, 65 (2001)
19. C. Rose-Petruck et al., Nature **398**, 310 (1999)
20. C. Rischel et al., Nature **390**, 490 (1997)
21. M.F. DeCamp et al., Nature **413**, 825 (2001)
22. P.E. Young et al., Phys. Rev. Lett. **61**, 2766 (1998)
23. R.P. Drake, R.E. Turner, B.F. Lasinski, E.A. Williams, W.L. Kent Estabrook, Kruer, E.M. Campbell, T.W. Johnston, Phys. Rev. A **40**, 3219 (1989)
24. D. Giulietti, D. Batani, V. Biancalana, A. Giulietti, L.A. Gizzi, $3\omega/2$, Il Nuovo Cimento **13D**, 845 (1991)
25. L.A. Gizzi, M. Galimberti, A. Giulietti, D. Giulietti, P. Koester, L. Labate, P. Tomassini, AIP Conf. Proc. **827**, 505–511 (2006)
26. L.A. Gizzi, A. Giulietti, D. Giulietti, P. Koester, L. Labate, T. Levato, F. Zamponi, T. Kämpfer, I. Uschmann, E. Förster, R. Sauerbre, SPIE Proc. **6634** (2007) (editor: S.B. Dabagov)
27. L.A. Gizzi, F. Anelli, C. Benedetti, C.A. Cecchetti, A. Clozza, G. Di Pirro, N. Drenska, R. Faccini, D. Giulietti, D. Filippetto, S. Fioravanti, A. Gamucci, L. Labate, T. Levato, V. Lollo, P. Londrillo, E. Pace, G. Turchetti, C. Vaccarezza, P. Valente, C. Vicario, Il Nuovo Cimento C, **32**, 433 (2009)
28. W.P. Leemans et al., Nat. Phys. **2**, 696 (2006)
29. V. Malka, J. Faure, Y.A. Gauduel, E. Lefebvre, A. Rousse, Kim Ta Phuoc Nat. Phys. **4**, 447–453 (2008)
30. L.A. Gizzi, A. Bacci, S. Betti, C.A. Cecchetti, M. Ferrario, A. Gamucci, A. Giulietti, D. Giulietti, P. Koester, L. Labate, T. Levato, V. Petrillo, L. Serafini, P. Tomassini, C. Vaccarezza, Eur. Phys. J. Spec Top **175**, 3–10 (2009)
31. P. Tomassini, A. Bacci, J. Cary, M. Ferrario, A. Giulietti, D. Giulietti, L.A. Gizzi, L. Labate, L. Serafini, V. Petrillo, C. Vaccarezza, IEEE Trans. Plasma Sci. **36**, 1782 (2008)
32. A. Bacci, F. Broggi, C. DeMartinis, D. Giove, C. Maroli, V. Petrillo, A.R. Rossi, L. Serafini, P. Tomassini, L. Cultrera, G. Di Pirro, M. Ferrario, D. Filippetto, G. Gatti, E. Pace, C. Vaccarezza, C. Vicario, F. Bosi, D. Giulietti, L.A. Gizzi, P. Oliva, Nucl. Instrum. Meth. Phys. Res, Sect. A **608**, S90 (2009)
33. M. Galimberti, J. Opt. Soc. Am. A **24**, 304–310 (2007)
34. L.A. Gizzi, M. Galimberti, A. Giulietti, D. Giulietti, P. Köster, L. Labate, P. Tomassini, Ph. Martin, T. Ceccotti, P. D'Oliveira, P. Monot, Phys. Rev. E **74**, 036403 (2006)
35. A. Giulietti, D. Giulietti, D. Batani, V. Biancalana, L. Gizzi, L. Nocera, E. Schifano, Phys. Rev. Lett. **63**, 524–527 (1989)
36. M. Galimberti et al., SHEEBA: a Spatial High Energy Electron Beam Analyzer. Rev. Sci. Instrum. **76**, 053303 (2005)

37. P. Tomassini, A. Giulietti, L.A. Gizzi, M. Galimberti, D. Giulietti, M. Borghesi, O. Willi, Appl. Opt. **40**, 6561 (2001)
38. P. Tomassini, A. Giulietti, Optics Comm. **199**, 143 (2001)
39. A. Giulietti, P. Tomassini, M. Galimberti, D. Giulietti, L.A. Gizzi, P. Köster, L. Labate, T. Ceccotti, P. D'Oliveira, T. Auguste, P. Monot, Ph. Martin, Phys. Plasmas **13**, 093103 (2006)
40. M. Takeda, H. Ia, S. Kobayashi, J. Opt. Soc. Am. **72**, 156 (1988)
41. D. Giulietti, L.A. Gizzi, La Rivista del Nuovo Cimento **21**, 1 (1998)
42. Lee et al., J. Quant. Spectrosc. Radiat. Transf. **32**, 91 (1984)
43. L.A. Gizzi, C.A. Cecchetti, M. Galimberti, A. Giulietti, D. Giulietti, L. Labate, S. Laville, P. Tomassini, Lett. Phys. Plasmas **10**, 4601 (2003)
44. L. Labate, C.A. Cecchetti, M. Galimberti, A. Giulietti, D. Giulietti, L.A. Gizzi, Phys. Plasmas **12**, 083101 (2005)
45. L.A. Gizzi, A. Giulietti, O. Willi, D. Riley, Phys. Rev. E **62**, 2721 (2000)
46. L.A. Gizzi, A.J. Mackinnon, D. Riley, S.M. Viana, O. Willi, Laser Part. Beams **13**, 511 (1995)
47. K. Lancaster et al., Phys. Rev. Lett. **98**, 125002 (2007)
48. F. Ewald, H. Schwoerer, R. Sauerbrey, Europhys. Lett. **60**, 710 (2002)
49. L.A. Gizzi, A. Giulietti, D. Giulietti, P. Köster, L. Labate, T. Levato, F. Zamponi, A. Lübcke, T. Kämpfer, I. Uschmann, E. Förster, A. Antonicci, D. Batani, Plasma Phys. Control. Fusion **49**, B211–B221 (2007)
50. L. Labate, M. Galimberti, A. Giulietti, D. Giulietti, L.A. Gizzi, P. Tomassini, G. Di Cocco, Nucl. Instr. Meth. A **495**, 148 (2002)
51. L. Labate, A. Giulietti, D. Giulietti, P. Koester, T. Levato, L.A. Gizzi, F. Zamponi, A. Luebcke, T. Kaempfer, I. Uschmann, E. Foerster, Rev. Sci. Instrum. **78**, 103506 (2007)
52. D. Strickland, G. Mourou, Opt. Commun. **56**, 212 (1986)